PNAS

Supporting Information for

Structural insights into the regulation of RyR1 by S100A1

Gunnar Weninger, Marco C. Miotto, Carl Tchagou, Steven Reiken, Haikel Dridi, Sören Brandenburg, Gabriel C. Riedemann, Qi Yuan, Yang Liu, Alexander Chang, Anetta Wronska, Stephan E. Lehnart, Andrew R. Marks

Gunnar Weninger

Email: gw2424@cumc.columbia.edu

Andrew R. Marks

Email: arm42@cumc.columbia.edu

This PDF file includes:

	Mouse RyR1	with apo-S100A1	with Ca-S100A1
Domain	**a.a.**	**RMSD (Å)**	**RMSD (Å)**
SPRY1-3	629-1657	0.35	0.44
CT-BSol	2950-3613	0.49	0.95
α-Helices in CT-BSol	2950-2984	0.29	0.79
	2992-3015	0.27	0.75
	3033-3052	0.24	0.76
	3054-3059	0.46	0.99
	3061-3084	0.28	0.79
	3086-3113	0.31	0.84
	3124-3152	0.34	0.86
	3160-3180	0.48	0.98
	3181-3202	0.40	0.93
	3124-3152	0.34	0.86
	3208-3216	0.61	1.15
	3224-3232	0.68	1.21
	3236-3242	0.52	0.91
	3246-3261	0.42	1.18
	3269-3289	0.45	0.98
	3309-3328	0.42	1.1
	3333-3348	0.42	0.84
	3353-3383	0.62	0.79
	3385-3418	0.57	0.81
	3420-3427	0.40	1.00
	3430-3449	0.36	1.01
	3451-3464	0.49	0.84
	3505-3527	0.53	1.03
	3528-3544	0.33	0.81
	3546-3558	0.56	0.81
	3569-3581	0.49	1.14
	3590-3612	0.36	0.85

Table S1. Sideways motion of the C-terminal BSol region upon binding of Ca-S100A1. RMSD values of the C-alpha backbone were calculated for the structures of RyR1 with apo- or Ca-S100A1 superimposed to the RyR1 controls (all particles). RMSD values for the SPRY1-3 region, CT-BSol region, and several α-helices in CT-BSol are depicted as indicated. RMSD values > 0.9 Å are highlighted in red. Compared to SPRY1-3, CT-BSol showed a substantially increased RMSD value upon binding of Ca-S100A1 but not for apo-S100A1.

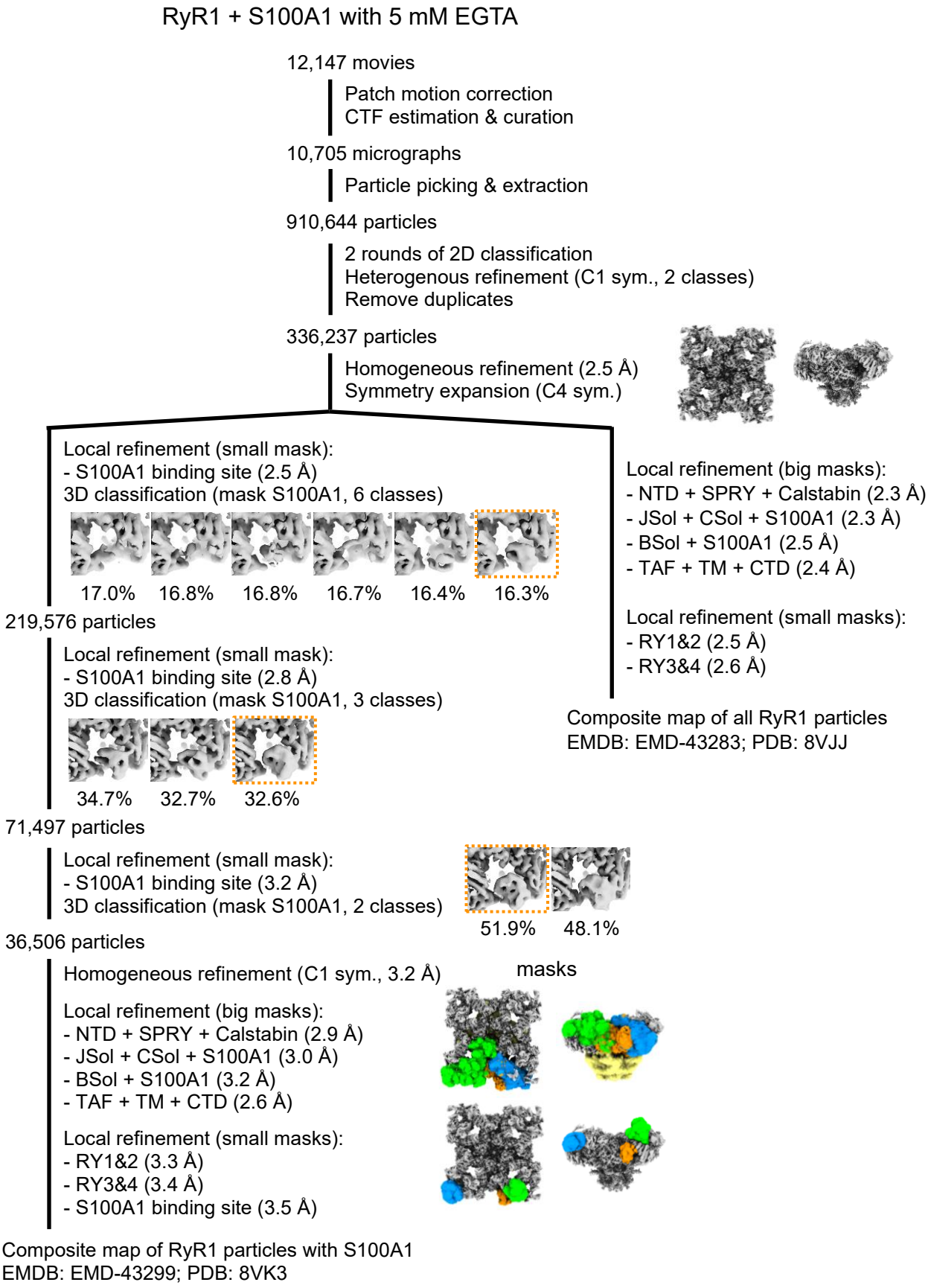

Figure S1. Processing workflow for the cryo-EM data set of RyR1 and S100A1 under EGTA condition performed in CryoSPARC v4.

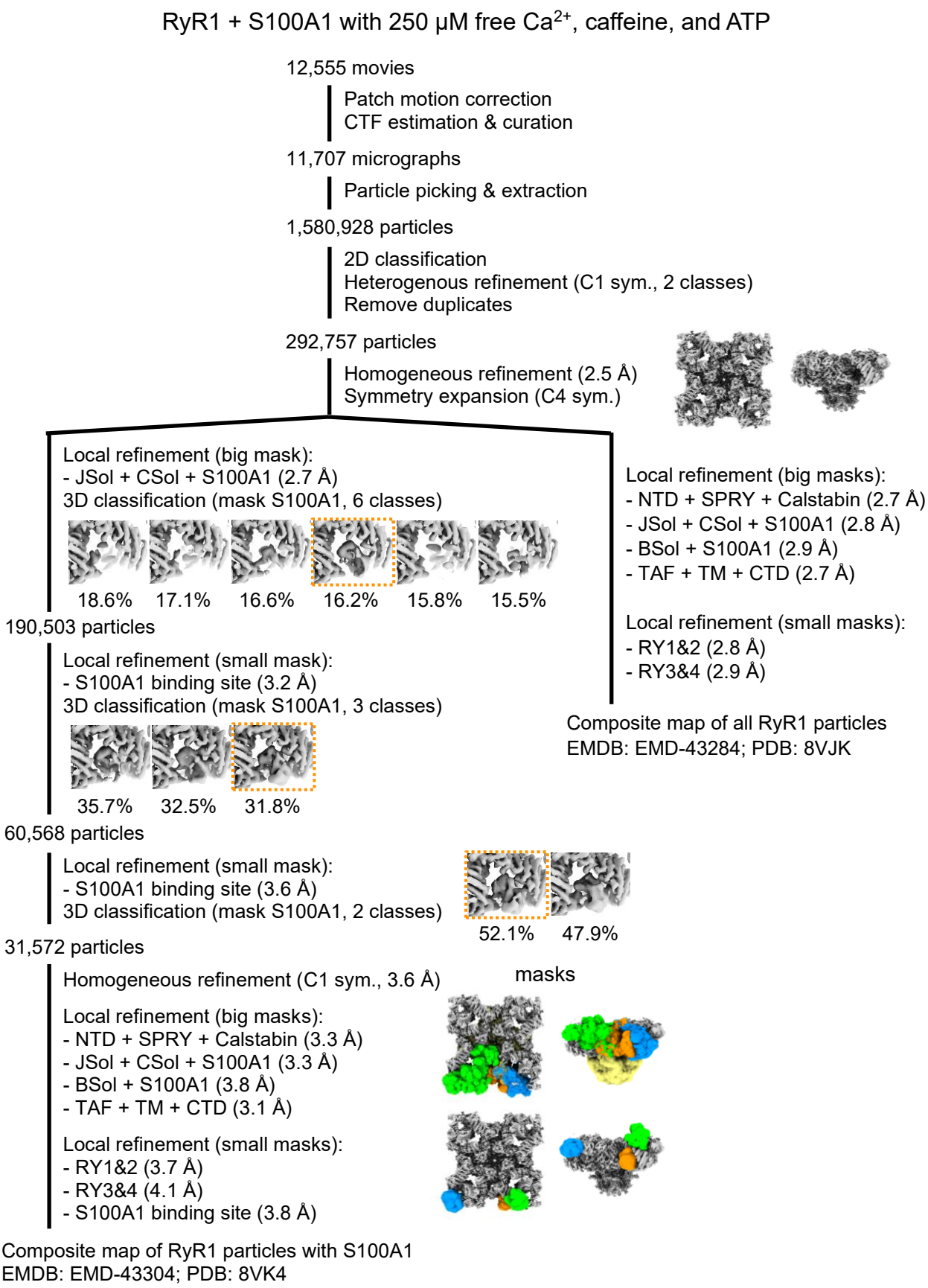

Figure S2. Processing workflow for the cryo-EM data set of RyR1 and S100A1 with 250 µM free Ca^{2+}, caffeine, and ATP performed in CryoSPARC v4.

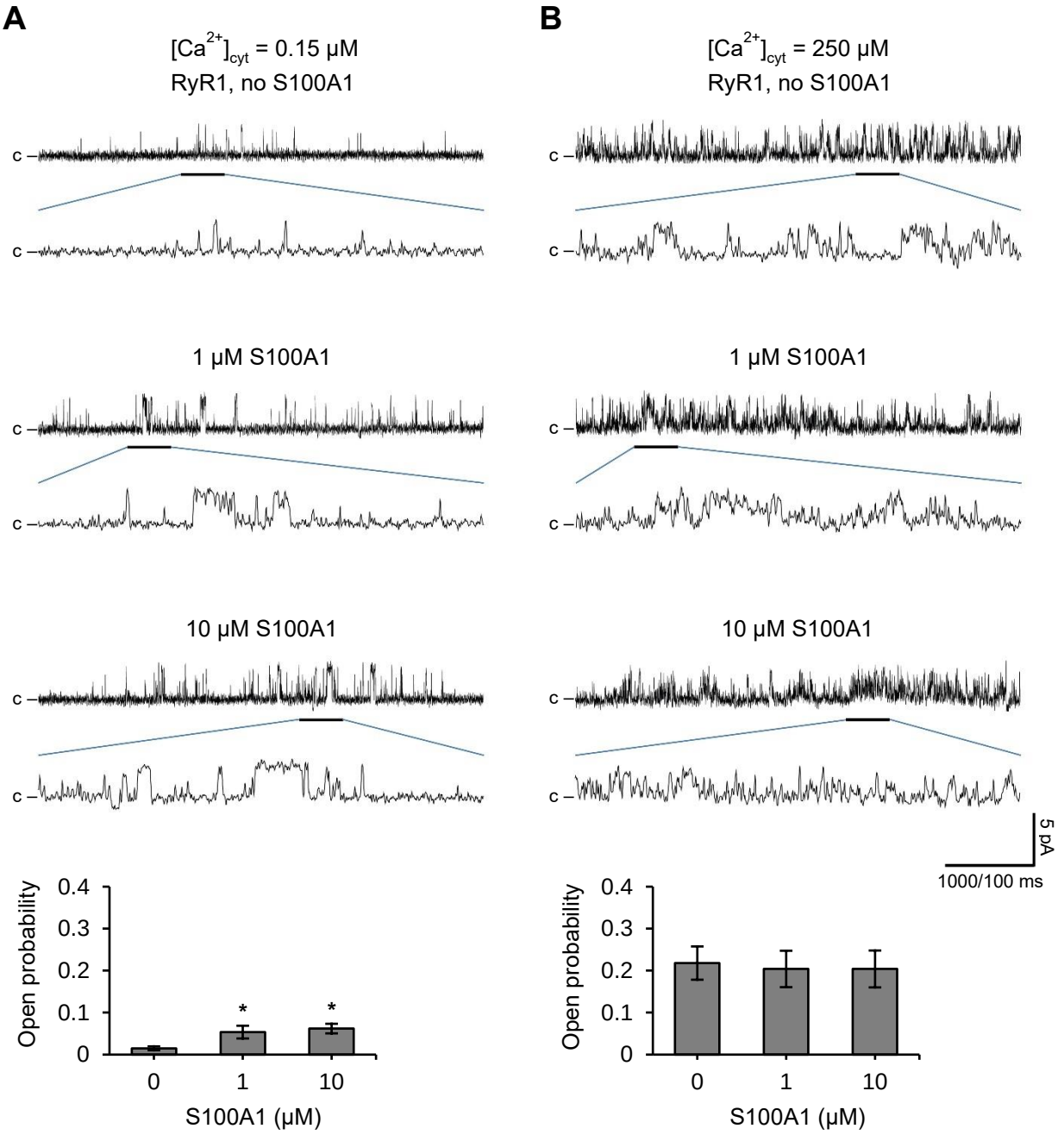

Figure S3. Single channel recordings of purified RyR1 (top) reconstituted in planar lipid bilayers at (A) 150 nM free Ca^{2+} or (B) 250 µM free Ca^{2+} and quantification of the open probability (bottom) of RyR1 with and without S100A1 (n=5 per group). Channel openings in current traces are represented as upward deflections from baseline (closed channel, c). Upon addition of 1 µM or 10 µM S100A1 at 150 nM free Ca^{2+}, the open probability (P_O) of RyR1 significantly increased from 0.01 to 0.05 or 0.07, respectively. At 250 µM free Ca^{2+}, S100A1 addition did not significantly alter P_O (~0.2). Two-tailed Student's t-test; *p < 0.05.

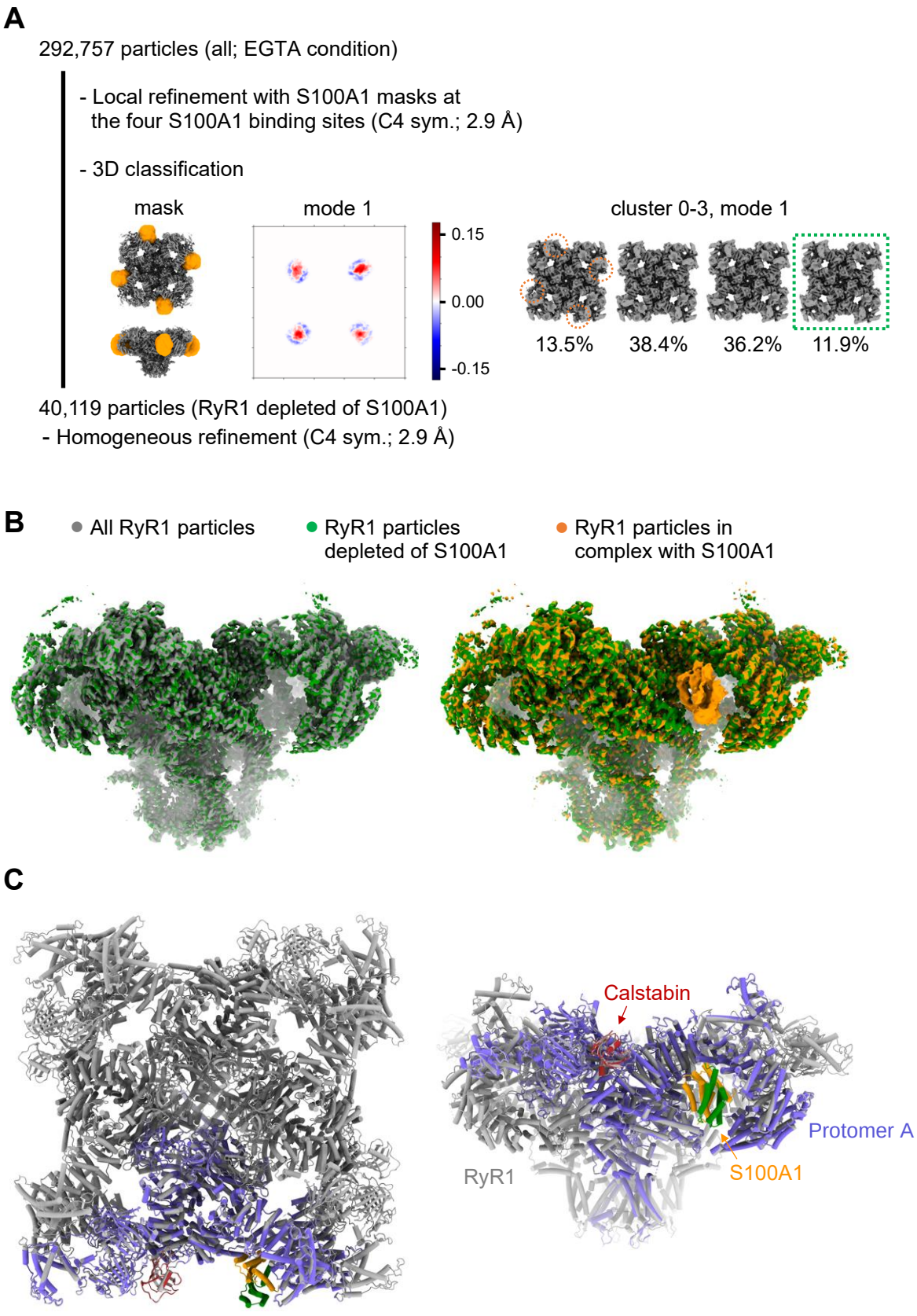

Figure S4. Structural comparison of RyR1 particles with and without apo-S100A1 under EGTA condition. (A) Selection of RyR1 particles without apo-S100A1 density by 3D variability (CryoSPARC) using a mask that separately covered the four S100A1 binding sites of the four RyR1 protomers. Mode 1 of the 3D variability analysis allowed to minimize S100A1 densities simultaneously in all four binding sites. A cluster of

40,119 RyR1 particles depleted in S100A1 density was selected from mode 1 and assessed by homogeneous refinement (global reconstruction at 2.9 Å resolution). (B) Superposition of cryo-EM maps after homogeneous refinements showing site views of RyR1 particles depleted of S100A1 density (green) versus all particles (grey; left panel) or versus RyR1-S100A1 particles (orange; right panel) selected by 3D classification (Figure S1). The RyR1 structures before (all particles) and after depletion of S100A1 density resemble each other. Hence, depletion of the S100A1 density by 3D variability did not significantly alter the structural conformation of RyR1. Moreover, the S100A1 density in all RyR1 particles is negligible compared to the RyR1-S100A1 particles. The RyR1 structures with and without apo-S100A1 show similar closed conformations under EGTA condition. (C) Top (left panel) and site views (right panel) of atomic models comparing RyR1 (all particles; grey; PDB: 8VJJ) with RyR1-S100A1 (colored; PDB: 8VK3; only one protomer shown) under EGTA condition. The comparison between both models does not reveal conformational changes in RyR1.

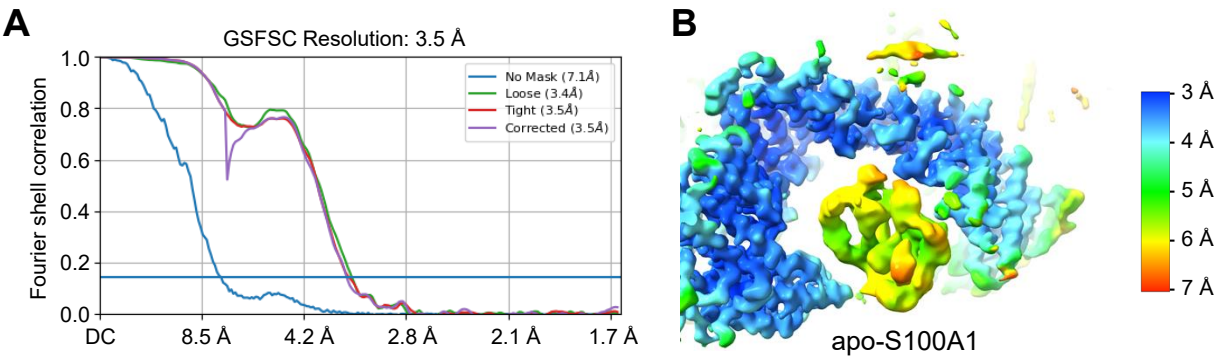

Figure S5. Gold-standard Fourier shell correlation curve and local resolution map for the apo-S100A1 binding site of RyR1. (A) Gold-standard Fourier shell correlation (FSC) curve calculated from two independent half-maps in the local refinement of the apo-S100A1 binding site (CryoSPARC). Overall, the resolution of the local reconstruction is ~3.5 Å (at FSC = 0.143). (B) Cryo-EM density map of the apo-S100A1 binding site colored according to estimated local resolutions (CryoSPARC) showing RyR1 at resolutions below 4 Å and apo-S100A1 at ~5-7 Å.

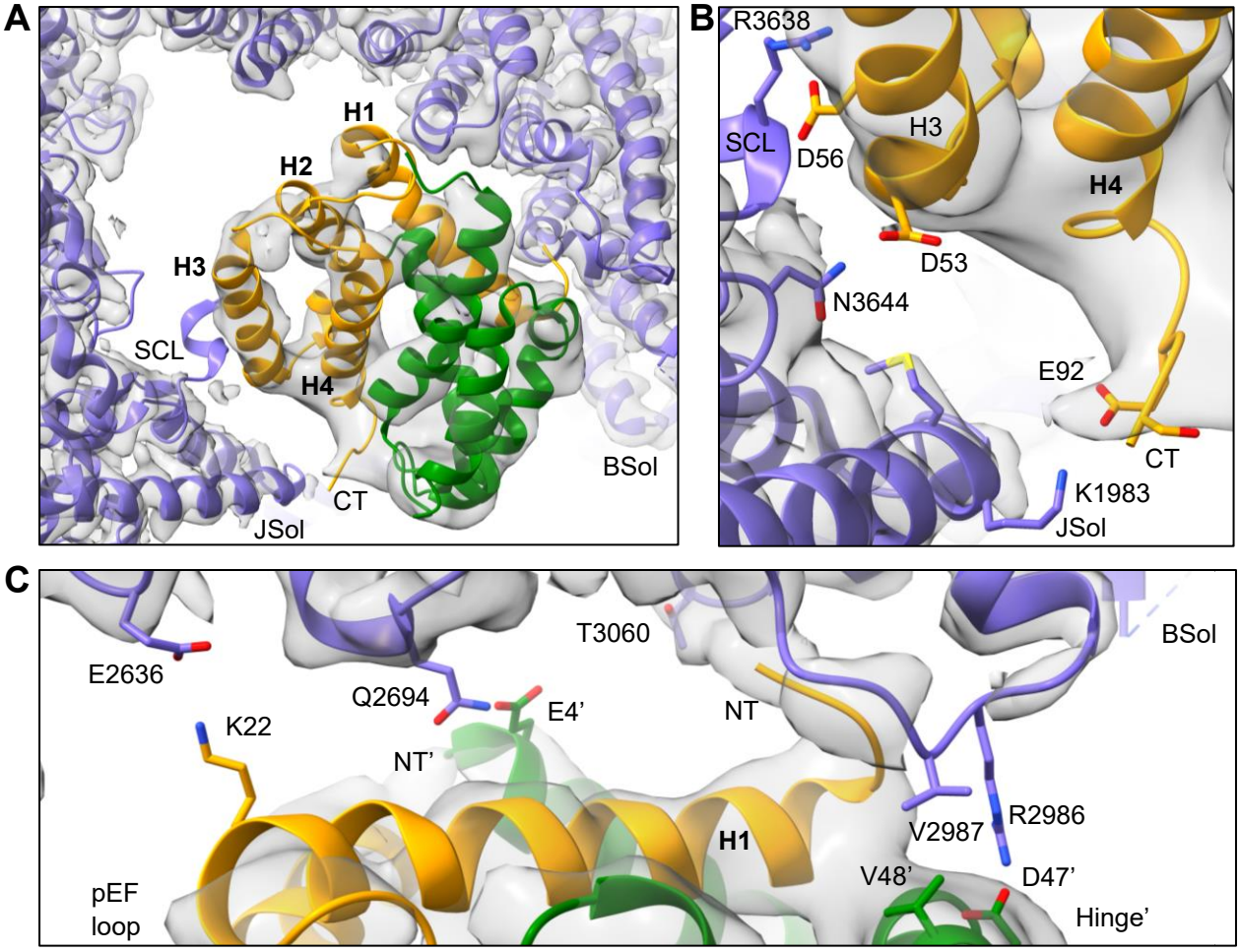

D

Mouse apo-S100A1			Mouse RyR1			Distance	Type
Residue	Atoms	Subunit (Chain)	Residue	Atoms	Protomer (Chain)	(Å)	
K22	NZ	1 (I)	E2636	OE1	A	3.1	SB
D53	OD1	1 (I)	N3644	ND2	A	2.6	HB
D56	OD1	1 (I)	R3638	NH2	A	1.6	SB
E92	OE2	1 (I)	K1983	NZ	A	2.9	SB
S94	OXT	1 (I)	K1983	NZ	A	3.4	HB
E4	OE2	2 (J)	Q2694	NE2	A	2.5	HB
D47	OD2	2 (J)	R2986	NH2	A	2.1	SB

Figure S6. Local interaction hot spots between RyR1 and apo-S100A1. (A) Overview of the apo-S100A1 binding site of RyR1 (cryo-EM map in grey). The monomeric subunits 1 (orange) and 2 (green) of homodimeric S100A1 and the surrounding binding site of RyR1 (violet) are depicted as ribbon models (PDB: 8VK3). (B) Interaction site between the JSol domain of RyR1 and the C-terminal region of S100A1-subunit 1. Adjacently, the shell-core linker (SCL) of RyR1 interacts with helix H3 of S100A1-subunit 1. (C) Interaction site between the BSol domain of RyR1 and helix H1 of S100A1-subunit 1. (D) Table of S100A1-RyR1 side chain interactions predicted by the

atomic model under EGTA condition. The listed H-bonds (HB) and salt bridges (SB) of side chains (depicted in B-C) are only putative, given limitations in resolution and potential dynamic changes of S100A1 binding.

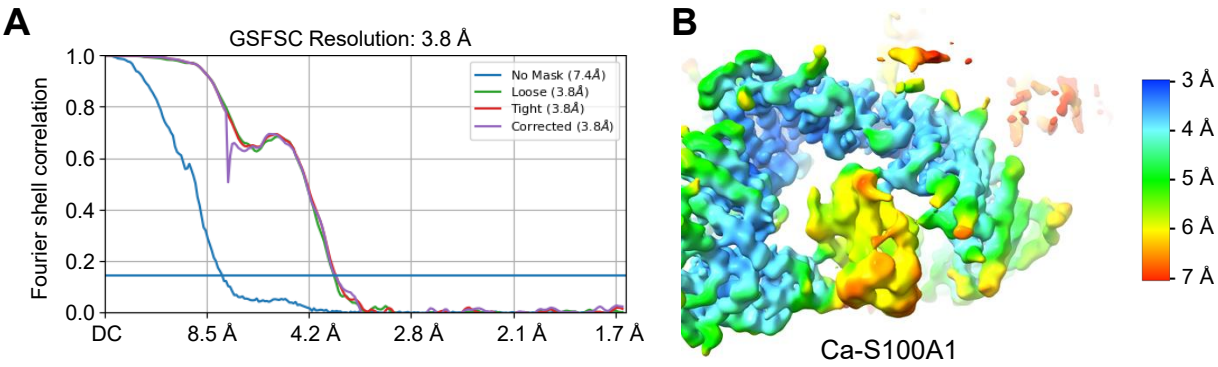

Figure S7. Gold-standard Fourier shell correlation curve and local resolution map for the Ca-S100A1 binding site of RyR1. (A) Gold-standard Fourier shell correlation (FSC) curve calculated from two independent half-maps in the local refinement of the Ca-S100A1 binding site (CryoSPARC). Overall, the resolution of the local reconstruction is ~3.8 Å (at FSC = 0.143). (B) Cryo-EM density map of the Ca-S100A1 binding site colored according to estimated local resolutions (CryoSPARC) showing RyR1 at ~3-5 Å and Ca-S100A1 at ~5-7 Å resolution.

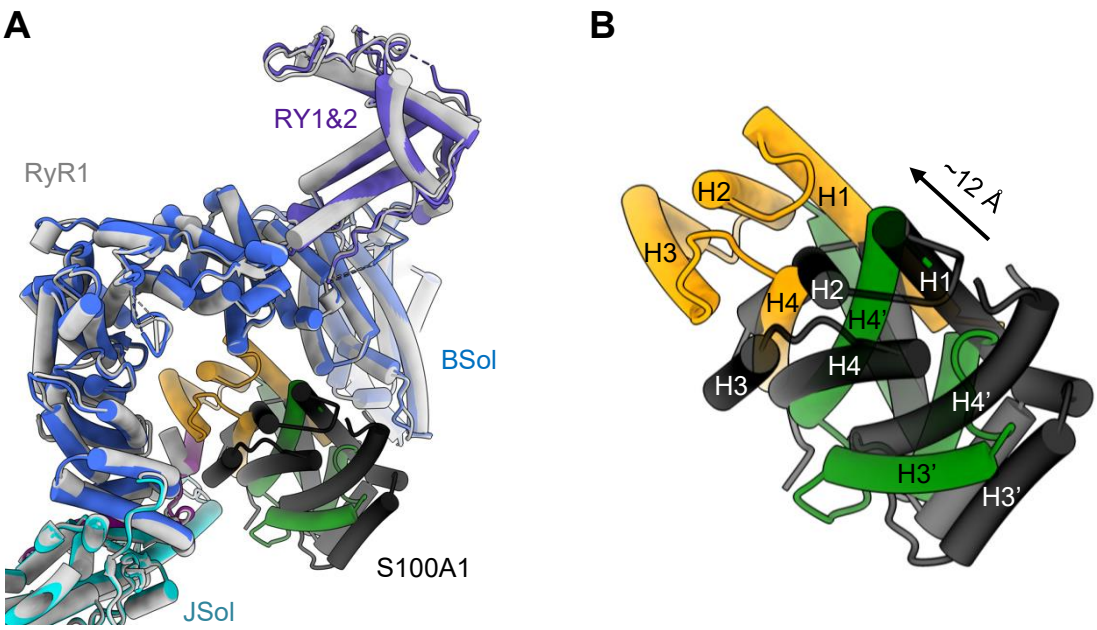

Figure S8. Structural comparison between the binding modes of apo-S100A1 and Ca-S100A1 on RyR1. (A) Superposition of RyR1 (grey) in complex with apo-S100A1 (black) versus RyR1 (colored) in complex with Ca-S100A1 (helices H1-H4 of subunit 1 in orange, helices H1'-H4' of subunit 2 in green). (B) Magnification showing the binding position of apo-S100A1 compared to Ca-S100A1. Upon Ca^{2+} binding, S100A1 changes its conformation and moves deeper beneath the BSol domain (A-B). The center-to-center distance between apo- and Ca-S100A1 is 12.0 Å and the C-alpha RMSD value 14.2 Å.

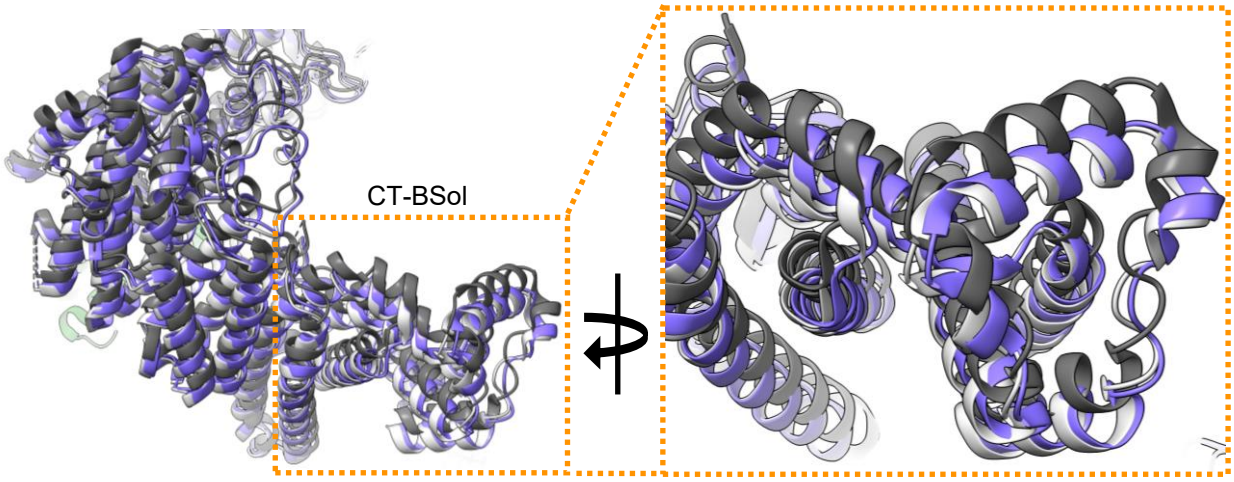

Figure S9. Sideways motion of the C-terminal BSol region upon binding of Ca-S100A1 versus downward motion induced by the small activating ligands ATP/Caffeine/Ca^{2+}. Side view on CT-BSol. Binding of the small activating ligands ATP, Caffeine, and Ca^{2+} to RyR1 (PDB: 8VJK; grey) induces a downward motion of CT-BSol compared to the EGTA condition (PDB: 8VJJ; black) while binding of Ca-S100A1 (PDB: 8VK4; colored) induces a sideways motion.

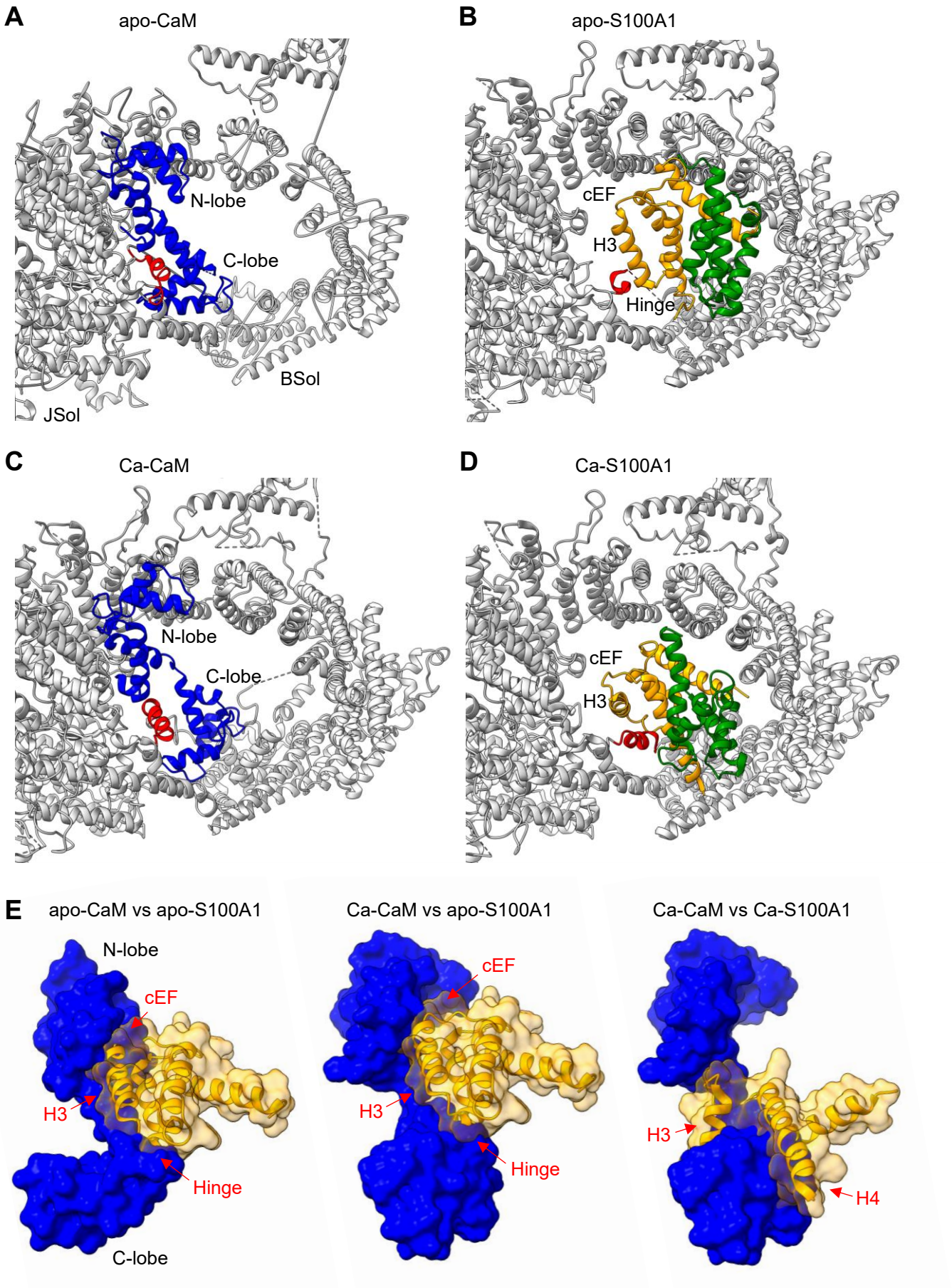

Figure S10. Structural comparison of CaM and S100A1 binding sites on RyR1 under Ca^{2+}-free and Ca^{2+}-bound conditions. (A-E) Atomic models of CaM (blue) and

homodimeric S100A1 (subunit 1 in orange, subunit 2 in green) bound to RyR1 (grey). Ca^{2+}-free and Ca^{2+}-saturated states are shown, namely RyR1 with (A) apo-CaM (PDB: 6X32), (B) apo-S100A1 (PDB: 8VK3), (C) Ca-CaM (PDB: 7TZC), and (D) Ca-S100A1 (PDB: 8VK4). The central helix (red) of the shell-core linker of RyR1 changes its orientation upon Ca-S100A1 binding (D) compared to the other RyR1 structures (A-C). (E) Steric overlap between CaM (blue surface) and subunit 1 of S100A1 (transparent orange surface and ribbon model). Left: apo-CaM versus apo-S100A1; middle: Ca-CaM versus apo-S100A1; right: Ca-CaM versus Ca-S100A1. Clashes between the protein models are indicated at the hinge region, helix H3, and cEF-loop of apo-S100A1 and helices H3-H4 of Ca-S100A1.

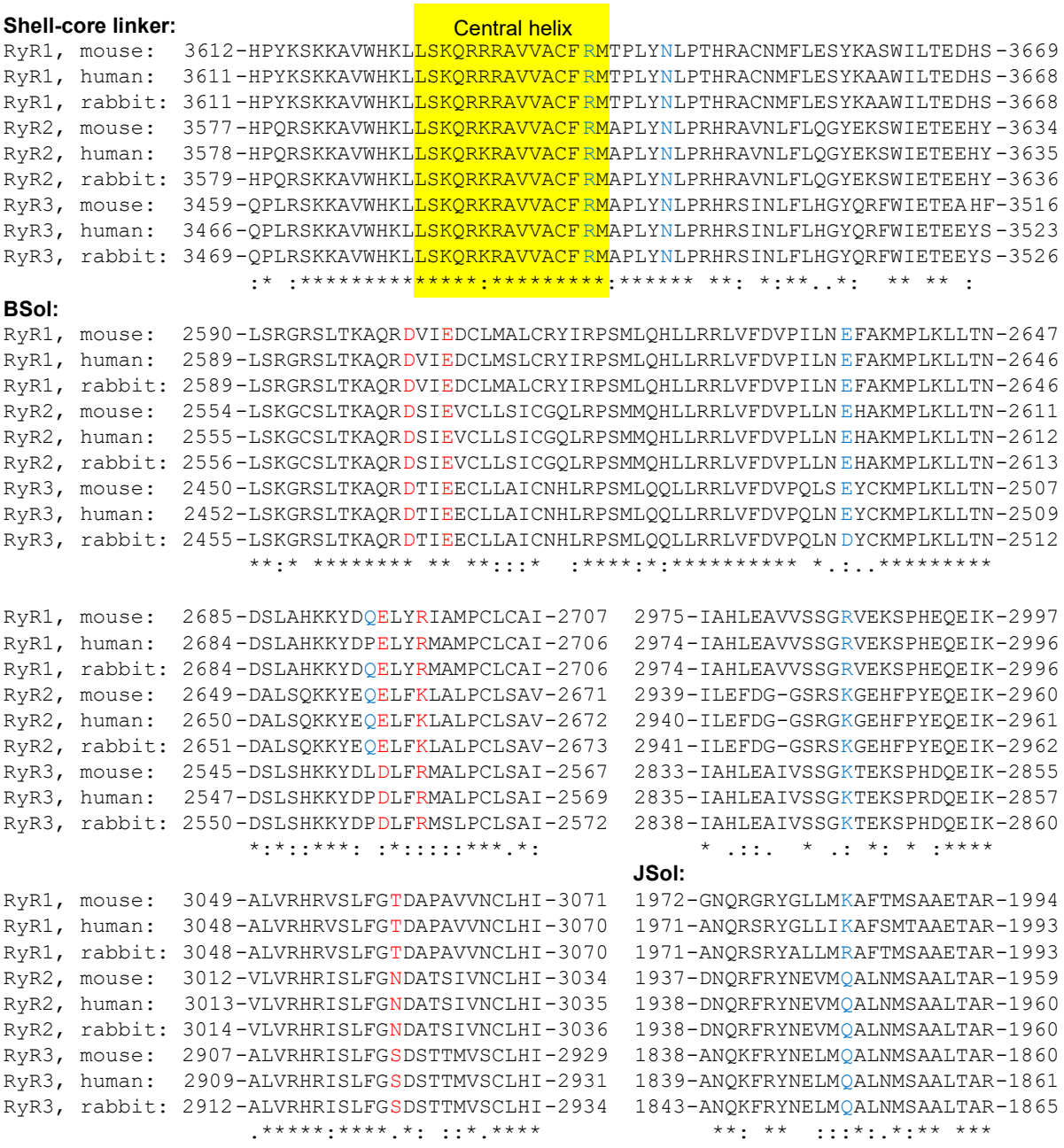

Figure S11. Evolutionary conservation of the S100A1 binding site on RyR1 across species and isoforms. Multiple sequence alignments of the RyR1, RyR2, and RyR3 isoforms from mouse, human, and rabbit are shown for sequence regions of the S100A1 binding site. Residues involved in putative H-bonds and salt bridges (Figure 2D and S6D) with apo-S100A1 (blue) or Ca-S100A1 (red) are located in conserved sequence regions of the shell-core linker, BSol, or JSol domain. The central helix (highlighted in yellow) of the shell-core linker that binds into the hydrophobic pocket of Ca-S100A1 exhibits a high conservation degree across RyR isoforms and species. Protein sequences from UniProt database: mouse RyR1, ID: E9PZQ0; human RyR1, ID: P21817-1; rabbit RyR1, ID: P11716; mouse RyR2, ID: E9Q401; human RyR2, ID: Q92736-1; rabbit RyR2, ID: P30957; mouse RyR3, ID: A2AGL3-1; human RyR3, ID: Q15413-1; rabbit RyR3, ID: Q9TS33-1. Asterisks, colons, and periods indicate identical residues, highly conserved residues, and semi-conserved residues, respectively.

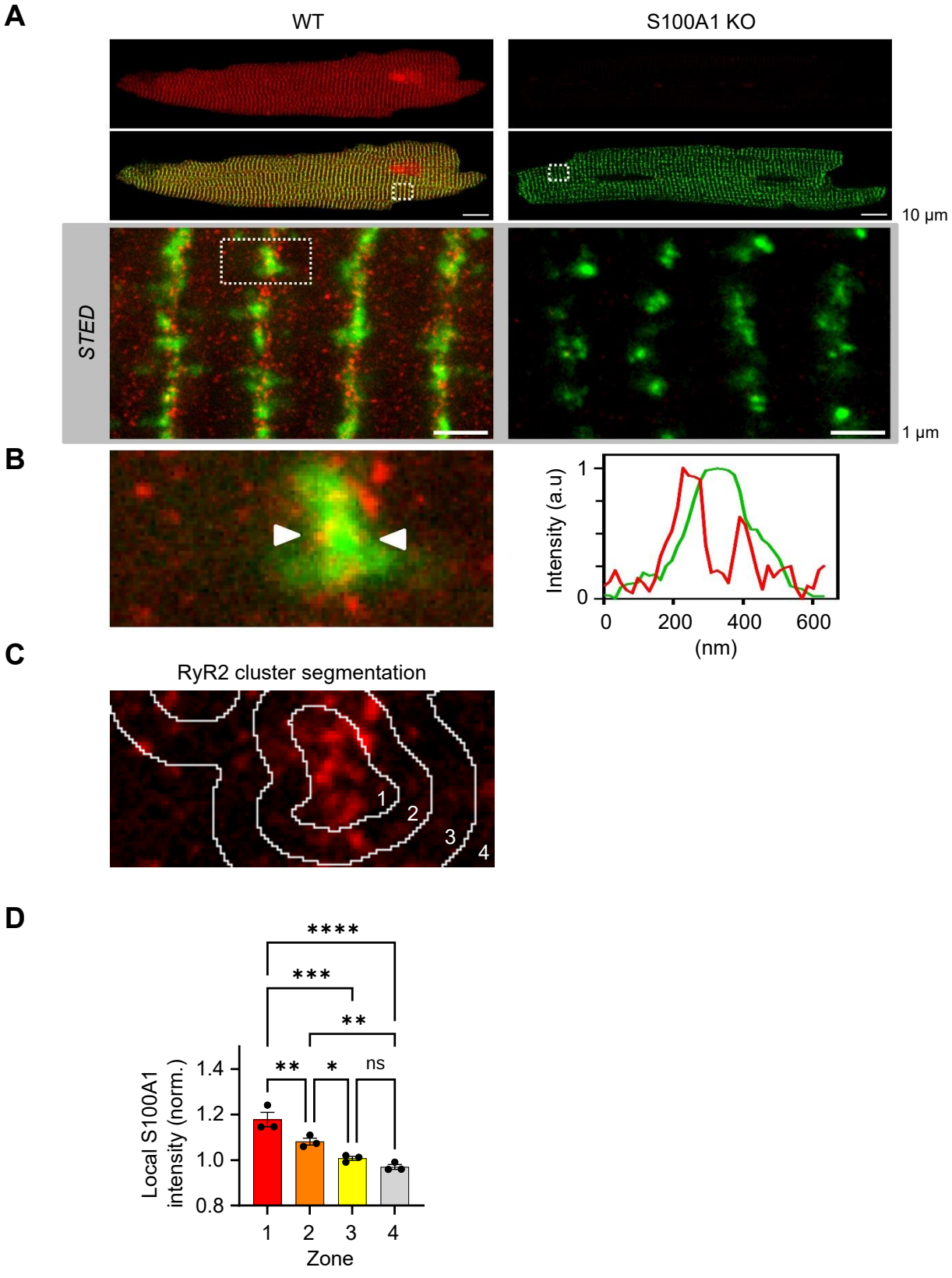

Figure S12. Co-immunofluorescence staining of S100A1 and RyR2 in ventricular cardiomyocytes isolated from WT and S100A1 KO mice. (A) In confocal and STED images, the immunofluorescence signal for S100A1 (red) was only detected in WT but not in S100A1 KO mice, while the immunofluorescence signal for RyR2 (green) showed similar RyR2 cluster arrangements in WT and S100A1 KO mice. In WT, both

RyR2 and S100A1 exhibited a cross-striated pattern typical for the sarcoplasmic reticulum. Dashed boxes indicate magnifications shown below. Scale bars, 10 µm (top) and 1 µm (bottom). (B) In the magnification, an exemplary RyR2 cluster is shown. As indicated by the line intensity profile, S100A1 signals were partially associated with RyR2 clusters. (C-D) Local S100A1 intensity analysis based on RyR2 cluster segmentation: (C) To assess the amount of S100A1 overlapping with or localizing at RyR2 clusters, RyR2 STED signals were segmented by previously published protocols (52-54). Zone 1 represents RyR2 clusters, zone 2 and 3 surrounding areas with 100 and 200 nm distance, respectively. Zone 4 indicates the intracellular cell periphery. (D) Dot plot showing the mean local S100A1 signal intensity in zone 1-4 normalized to the whole cell intensity, demonstrating a gradual increase of S100A1 signal intensity in proximity to RyR2 clusters. *n* = 3 mice, 9 ventricular cardiomyocytes. One-way ANOVA with post-hoc Tukey testing; *p < 0.05; **p < 0.01; ***p < 0.001; ****p < 0.0001.

Co-pull-down of GST-S100A1 and RyR1 under EGTA or Ca^{2+} condition, replicates 1-6

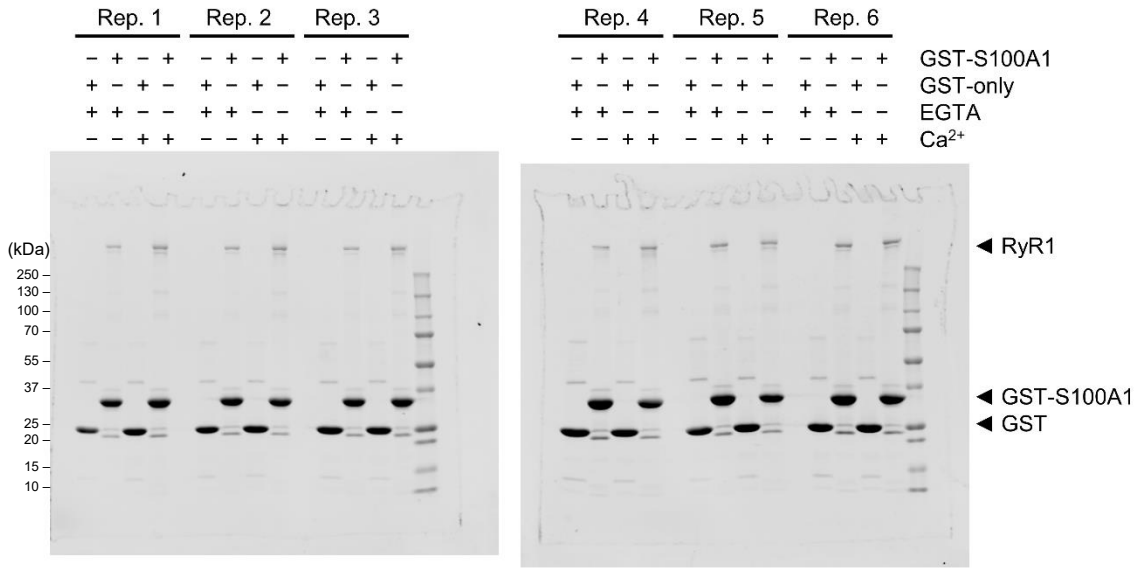

Figure S13. Original blot and gel images (1/3). Complementary original images to figure 1A-B showing GST pull-down assays of GST-tagged S100A1 and RyR1. Eluted samples were subjected to SDS-PAGE followed by Coomassie staining. Co-pull-down of RyR1 with GST-S100A1 was observed under apo (1 mM EGTA) and Ca^{2+}-saturated conditions (1 mM free Ca^{2+}) confirming the interaction between both proteins. GST-only served as negative control. Six biological replicates were prepared for the statistical quantification of the GST pull-down assays shown in figure 1B.

IP of RyR from cerebellar and heart lysates with EGTA-only or 10 µM free Ca^{2+}, replicates 1-4

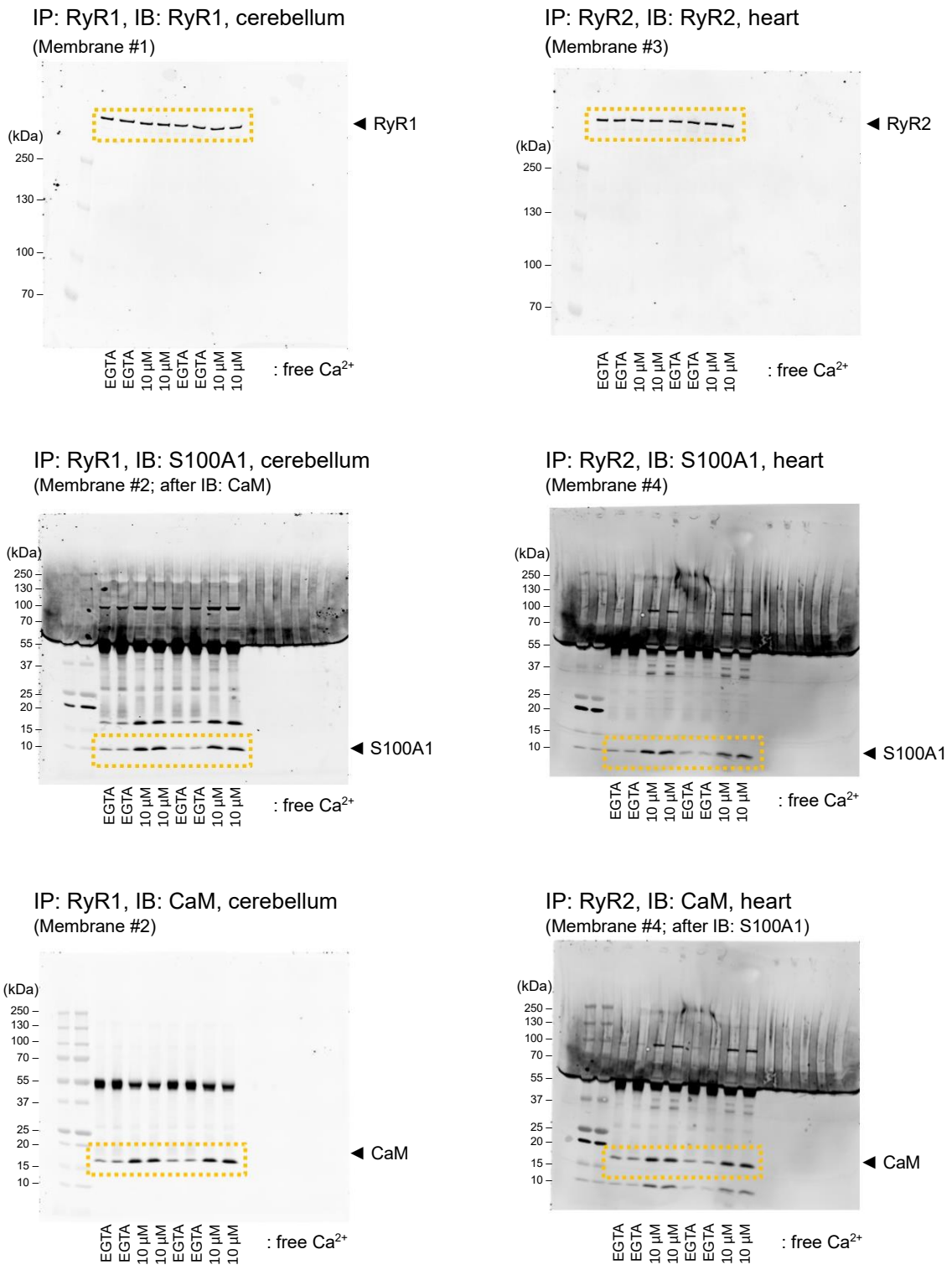

Figure S13. Original blot and gel images (2/3). Complementary original images to figure 6B showing co-immunoprecipitations (IP) between endogenous RyR channels and S100A1 versus CaM. RyR complexes were immunoprecipitated from heart muscle or cerebellar lysates at indicated free [Ca^{2+}] followed by immunoblotting (IB) against RyR, S100A1, and CaM. Protein bands of interest are indicated.

IP of RyR1 from skeletal muscle lysates at different free Ca^{2+} concentrations, replicates 1-6

IP: RyR1, IB: RyR1, skeletal muscle

(Membrane #5; IB: RyR1) (Membrane #8; IB: RyR1) (Membrane #10; IB: RyR1)

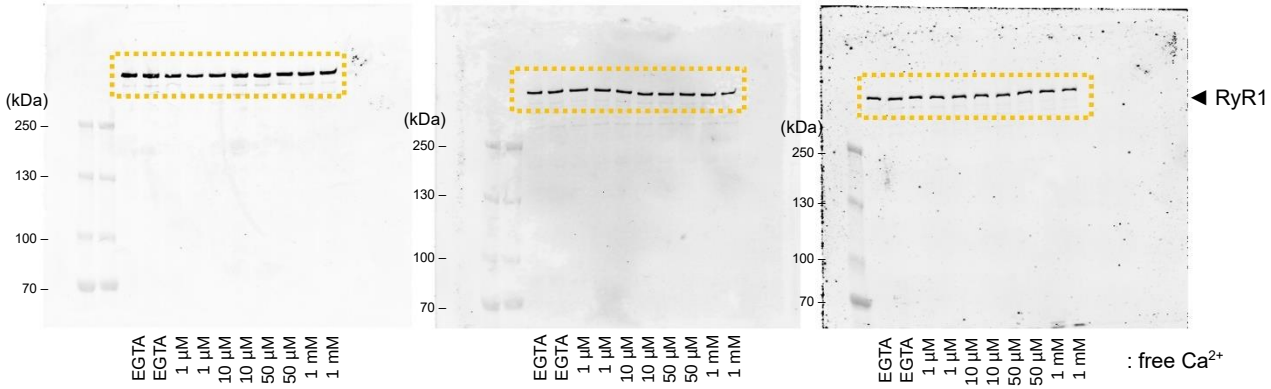

IP: RyR1, IB: S100A1, skeletal muscle

(Membrane #6; IB: S100A1) (Membrane #9; IB: S100A1 + IB: CaM) (Membrane #11; IB: S100A1)

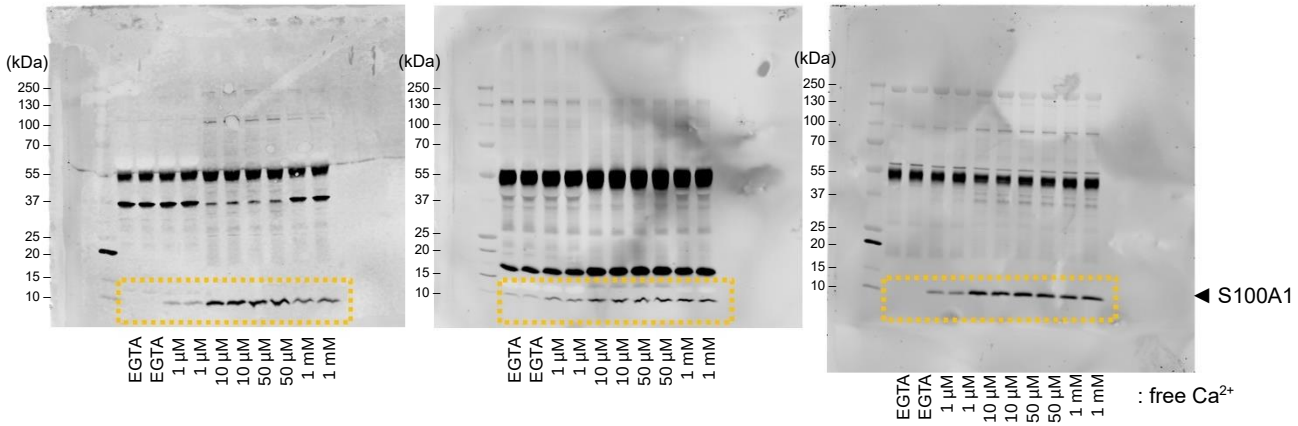

IP: RyR1, IB: CaM, skeletal muscle

(Membrane #7; IB: CaM) (Membrane #9; IB: S100A1 + IB: CaM) (Membrane #12; IB: CaM)

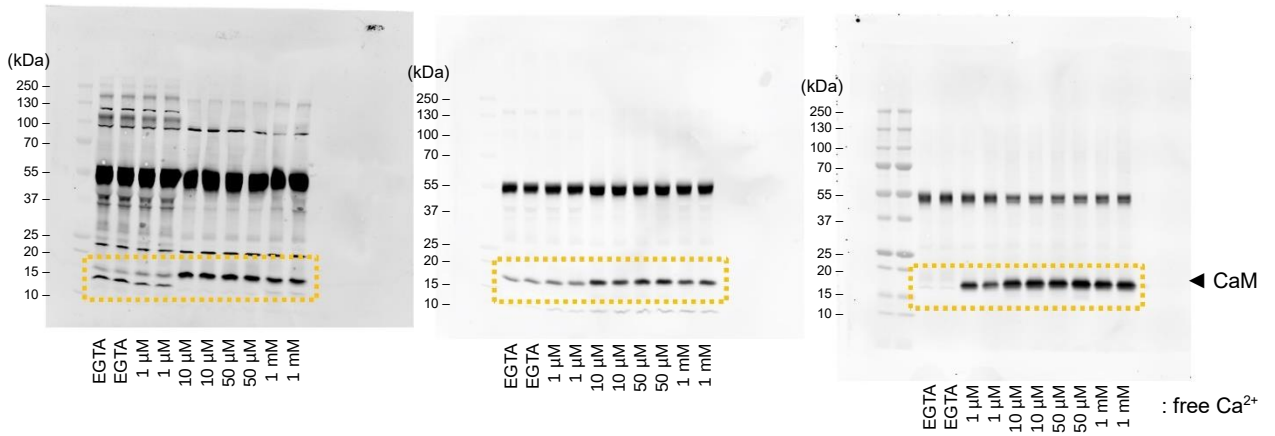

IP of RyR1 from skeletal muscle lysates at different free Ca^{2+} concentrations, replicates 7-8; blots including chromatographically purified RyR1, CaM, and S100A1 as IB positive controls

IP: RyR1, IB: RyR1, skeletal muscle
(Membrane #13)

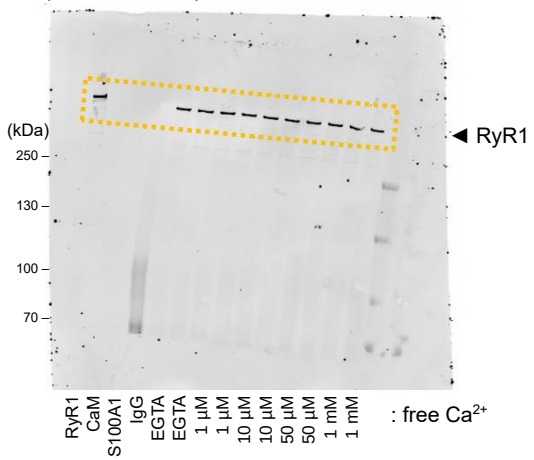

IP: RyR1, IB: S100A1, skeletal muscle
(Membrane #14; after IB: CaM)

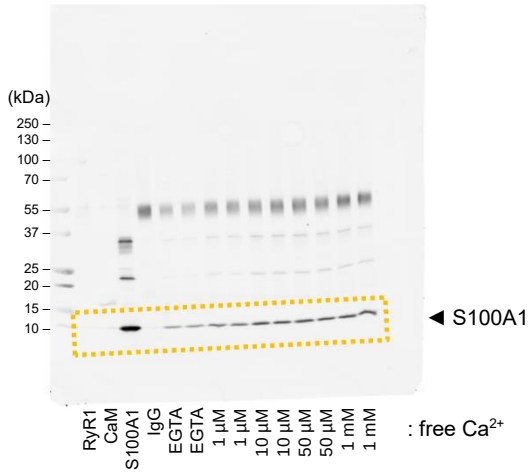

IP: RyR1, IB: CaM, skeletal muscle
(Membrane #14)

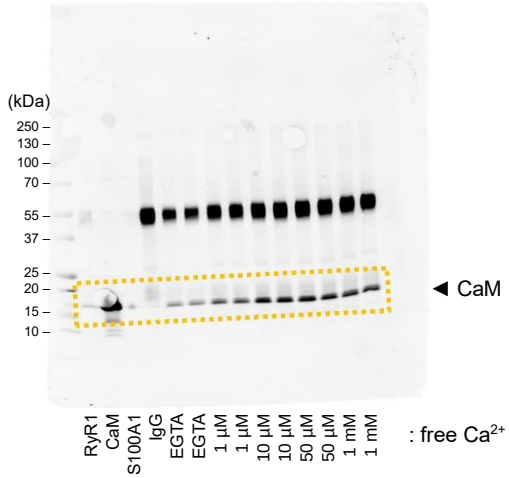

Figure S13. Original blot and gel images (3/3). Complementary original images to figure 6B-C showing co-immunoprecipitations (IP) between endogenous RyR1 channels and S100A1 versus CaM. RyR1 complexes were immunoprecipitated from skeletal muscle lysates at indicated free [Ca^{2+}] followed by immunoblotting (IB) against RyR1, S100A1, and CaM. Non-specific normal rabbit immunoglobulin G (IgG) served as negative control antibody in RyR1 IPs. Chromatographically purified RyR1, S100A1, and CaM were used as positive controls to confirm antibody specificities in immunoblots. Protein bands of interest are indicated. Eight biological replicates were prepared for the statistical quantification of the co-immunoprecipitations shown in figure 6C.